Journal of
Materials Chemistry C
Materials for optical, magnetic and electronic devices

This article can be cited before page numbers have been issued, to do this please use: G. N. Antoniou, P. Yuan, L. Koutsokeras, S. ATHANASOPOULOS, D. Fazzi, J. Panidi, D. G. Georgiadou, T. Prodromakis and P. E. Keivanidis, *J. Mater. Chem. C*, 2022, DOI: 10.1039/D2TC00662F.

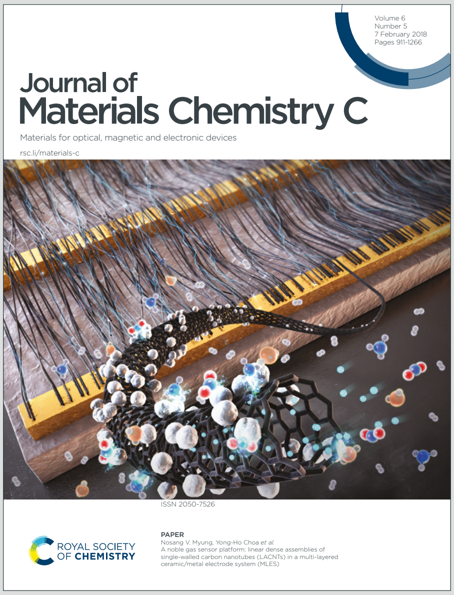

Volume 6
Number 5
7 February 2018
Pages 911-1266

Journal of
Materials Chemistry C

Materials for optical, magnetic and electronic devices

rsc.li/materials-c

ISSN 2050-7526

ROYAL SOCIETY
OF CHEMISTRY

PAPER
Nosang V. Myung, Yong-Ho Choa *et al.*
A noble gas sensor platform: linear dense assemblies of single-walled carbon nanotubes (LACNTs) in a multi-layered ceramic/metal electrode system (MLES)

ROYAL SOCIETY
OF CHEMISTRY

rsc.li/materials-c

View Article Online
DOI: 10.1039/D2TC00662F

ARTICLE

Low-power supralinear photocurrent generation via excited state fusion in single-component nanostructured organic photodetectors

Received 00th January 20xx,
Accepted 00th January 20xx

DOI: 10.1039/x0xx00000x

Giannis Antoniou [a], Peisen Yuan [a], Loukas Koutsokeras [a], Stavros Athanasopoulos [b], Daniele Fazzi [c], Julianna Panidi [d], Dimitra G. Georgiadou [d], Themis Prodromakis [d], Panagiotis E. Keivanidis *[a]

The integration of triplet-triplet annihilation (TTA) components as electrically and optically active elements in vertically-configured photoactive device architectures is a challenging task to achieve. Herein we present a simple methodology for incorporating a photon absorbing layer of the (2,3,7,8,12,13,17,18-octaethyl-porphyrinato) platinum (II) (PtOEP) metallorganic complex, as a self-TTA annihilator medium in a sandwich-like photodiode device structure. At low power illumination, the PtOEP photodiode exhibits photocurrent generation via the fusion of optically induced PtOEP excited states and it develops an open-circuit voltage (V_{OC}) as high as 1.15 V. The structural and spectroscopic characterization of the nanostructured PtOEP photoactive layer in combination with electronic structure calculations identify PtOEP dimer species as the annihilating excited state responsible for the formation of charges. The participation of the fusion process in the mechanism of charge photogeneration manifests in the supralinear dependence of the short-circuit current density (J_{SC}) on the incoming photoexcitation intensity, both when incoherent and coherent light is used for illuminating the PtOEP diodes. The photoresponse of the PtOEP device allows for the highly selective and sensitive photodetection within the 500 - 560 nm narrow spectral range. At short-circuit conditions a power-law is observed in the dependence of the device responsivity on fluence. The observed response of the PtOEP photodiodes reveals a hitherto neglected mechanism of photocurrent generation in single-component organic electronic devices that is facilitated by TTA reactions. Our findings pave the way towards the fabrication of next-generation electro-optical switches, ultrasensitive organic photodetectors, and TTA-sensitized solar cells with vertically configured device structure.

Introduction

Organic semiconductor materials represent a leading class of next generation molecular systems that have revolutionized the field of optoelectronic devices and have established a range of transforming technologies such as light emitting diodes (LEDs), [1] field effect transistors (FETs), [2] photovoltaic (PV) [3] and photodetector devices. [4] Since the advent of molecular crystals, the formation of carriers by light absorption in π-conjugated organic materials has been the topic of intensive research. [5] Small-molecule and polymeric material structures containing sp^2-hybridized carbon atoms exhibit high absorption coefficients, thereby undergoing highly allowed electronic transitions via one-photon absorption steps that result in the formation of excitonic states.

Especially for the case of vertically-configured photoactive device architectures that aim to light detection *i.e.* organic photodetector devices (OPDs), charge photogeneration is of paramount importance to their performance. Similar to organic solar cell (OSC) devices, the excitons formed in the photoactive layers of OPDs serve as precursors of charge transfer (CT) states that facilitate charge photogeneration. [6] Owing to the relatively large exciton binding energy in organic semiconductors, exciton dissociation is rarely spontaneous and it is achieved with the aid of a driving force that facilitates the activation of CT states. [7, 8] The formation of partially separated electron-hole pairs is facilitated by heterojunctions in the photoactive layer between the organic molecule and another molecule that is either in the form of unwanted impurities [9] or deliberately placed species. In these heterojunctions the alignment between the highest occupied molecular orbitals (HOMO) and the lowest unoccupied molecular orbitals (LUMO) of the two blend components should form a type-II heterojunction. As such, the second component in the blend is capable to accept an electron (hole) from the LUMO (HOMO) level of the photoexcited organic material. [10] In the absence of heterojunctions, intrinsic charge photogeneration is inefficient and may occur by i) the compensation of the exciton binding energy with the application of an external electric field, [11, 12] ii) offsets in the electrostatic potential in the photoactive layer due to the different structural organization of the organic material [13], or iii) non-linear light absorption processes induced by two-photon or sequential photon absorption. [14, 15]

---

[a] Device Technology and Chemical Physics Laboratory, Department of Mechanical Engineering and Materials Science and Engineering, Cyprus University of Technology, 45 Kitiou Kyprianou str., Limassol 3041, Cyprus
[b] Departamento de Física, Universidad Carlos III de Madrid, Avenida Universidad 30, 28911 Leganés, Madrid, Spain
[c] Dipartimento di Chimica "Giacomo Ciamician", Università di Bologna, via F. Selmi, 2, 40126 Bologna, Italy
[d] Centre for Electronics Frontiers, Electronics and Computer Science, University of Southampton, Highfield Campus, University Road, Building 53 (Mountbatten), Southampton SO17 1BJ, United Kingdom

Electronic Supplementary Information (ESI) available: UV-Vis absorption spectra of the spin-coated PS:PtOEP 10 wt% and the thermally evaporated PtOEP films, dark current J-V curve of the hole-only device with a thermally evaporated PtOEP layer. See DOI: 10.1039/x0xx00000x

During the last years one-photon absorption OPD platforms have demonstrated a remarkable progress.[16-18] Irrespective of the way charges are formed in OPDs, the main figures of merit to be considered are the device responsivity (R), the dark leakage current ($\boldsymbol{i_d}$), the noise-equivalent power (NEP) and the specific detectivity (D^*). The R parameter corresponds to the ratio of the registered photocurrent density ($\boldsymbol{J_{ph}}$) to the incident light intensity ($\boldsymbol{I_{exc}}$); that is $R=\frac{J_{ph}}{I_{exc}}$.[17, 19] Assuming that the dark leakage current dominates over the thermal noise current of the OPD device, the overall noise current ($\boldsymbol{i_n}$) under 1 Hz operation is $\boldsymbol{i_n}=\sqrt{\boldsymbol{2qi_d}}$. The NEP parameter represents the lowest incident light power at which no discernible output photocurrent signal can be obtained; that is $NEP=\frac{i_n}{R}$.[18, 20, 21] Consequently, the specific detectivity D^* quantifies the ability of the photodetector to respond to low level incident light power, independently of the device photoactive area (A), and it is expressed as $D^*=\frac{\sqrt{A}}{NEP}$.[22, 23]

Recent reports have presented high-performance bulk heterojunction donor/acceptor OPD layers of subphthalocyanine derivatives[24] that exhibit low dark current density ($J_d=\frac{i_d}{A}$) and high R values in the order of 53.1 nA cm^{-2} and 250 mA W^{-1}, respectively. Fullerene-free OPDs deliver state-of-the-art NEP values of 0.22 × pW Hz$^{-1/2}$ under 532 nm illumination[25] and D^* values as high as 3.3×10^{11} Jones at 560 nm photoexcitation.[20] Further progress is noted recently by covalently linking the donor and the acceptor components of the OPD layer in order to achieve a single component OPD photoactive layer.[26] For those OPDs the detection of 633 nm light with intensity of 500 μW cm^{-2} was achieved with an R of 0.9 mA W^{-1} while D^* was ~ 2×10^9 Jones.

Contrary to the cases of one-photon absorption devices, not much attention has been paid to OPDs that exhibit non-linear photocurrent generation via multiphoton absorption schemes. This is attributed mainly to the rather complicated setups that require the use of ultrashort *i.e.* fs, and high-repetition laser pulses to establish the proper conditions that facilitate the two-photon or sequential photon absorption transitions. Nevertheless, the technological significance of non-linear photodetectors has been recognized.[27] An alternative approach for realizing non-linear OPDs without necessarily employing high-power ultrafast pulsed laser sources would be the utilization of excited state fusion reactions that in principle can support the activation of CT states[28-30] via autoionization. By establishing a platform to facilitate supralinear photocurrent generation under low power lighting, an advancement in the technology of radiation sensing is to be expected, *i.e.* via the fabrication of inexpensive carbon-based electrooptical switches for ultrasensitive photodetection applications, and the development of light-modulated photodetecting organic FETs.

In this work we set out to explore the possibility to enable photocurrent generation via the fusion of long-lived excited states in photodiodes of the (2,3,7,8,12,13,17,18-octaethyl-porphyrinato) platinum (II) (PtOEP) phosphorescent dye; a disk-shaped metallo-organic complex that is a well-established triplet-emitter in organic electronics.[31] The long-lived triplet excited state of PtOEP offers the opportunity to achieve a supralinear photoresponse by employing less demanding optical photoexcitation schemes, *i.e.* incoherent light sources or low-power, continuous-wave (CW) monochromatic laser photoexcitation. For our work we focus on a vertically-configured OPD device platform with a thermally evaporated PtOEP photoactive layer.

The absorption spectrum of PtOEP layer lies within the visible spectral range and its absorption edge is located at about 640 nm. By photoexciting the PtOEP complex at shorter wavelengths (500 – 600 nm, Q-band) the first singlet excited state (S_1) is populated.[32, 33] In presence of the Pt heavy atom, the efficient spin–orbit coupling between the singlet and triplet manifolds facilitates the fast intersystem-crossing from S_1 to the triplet excited state (T_1), generating phosphorescence. Based on the peak intensity of the characteristic PtOEP phosphorescence, the energy of the first triplet excited level is placed at T_1= 1.9 eV.[32, 33] In addition, PtOEP possesses a deep HOMO level that is energetically located at -5.3 eV,[34, 35] thereby making PtOEP suitable to facilitate hole extraction at the hole-collecting electrode of a photodiode device structure. Owing to its long-lived triplet excited state, PtOEP has the capability to undergo triplet-triplet annihilation (TTA) reactions and to store photon energy in a TTA-mediated higher lying PtOEP state.[36-41] It is therefore meaningful to consider PtOEP as an ideal material for establishing TTA-driven charge photogeneration. Being electronically coupled in a photodiode configuration, PtOEP can undertake simultaneously the roles of photon absorbing, TTA annihilating, charge generating and charge transporting material.

Concerning charge transport, p-channel organic FETs with epitaxially grown PtOEP layers have been demonstrated[42] where hole mobility was found to be as high as $\mu_{FET} = 2.2 \times 10^{-4}$ cm^2 V^{-1}s^{-1}. In disk-shaped metallo-porphyrin complexes charge transport takes place along the π-π stacking direction of the porphyrin macrocycles. While in amorphous metallo-porphyrin films hole mobility is limited by trapping sites,[43] the development of well-structured porphyrin assemblies[44] can improve stacking along the π-π direction. Earlier studies have proposed the use of porphyrin complexes for charge photogeneration via triplet exciton dissociation.[45] With regard to photoconductivity, PtOEP photodiodes have been studied in symmetric vertical device configurations equipped with semitransparent aluminum (Al) electrodes.[46] In those systems, the propensity of PtOEP to photo generate charges was monitored in ambient atmosphere and at room temperature after photoexciting the PtOEP photodiodes with incoherent light, while applying an electric field of 1.5×10^5 V cm^{-1}. Photoconductivity in PtOEP devices was attributed to the dissociation of PtOEP triplet excitons that proceeds according to the Onsager theory of geminate charge recombination.[10] The short-circuit current density (J_{SC}) of those photodiodes was found to follow a linear-to-square root dependence on light fluence, and the observed transition was understood as the outcome of photocurrent losses due to bimolecular charge recombination when fluence exceeded the threshold of 10^{14} cm^{-2}s^{-1}.

At present, we demonstrate the capability of PtOEP photodiodes to support photocurrent generation via excited state fusion that manifests in the supralinear dependence of photocurrent density on photoexcitation. When a 532 nm CW-laser source is used, the obtained J_{SC} and open-circuit voltage (V_{OC}) of the PtOEP-photodiodes become as high as 0.24 mA cm^{-2} and 1.15 V, respectively. These results demonstrate a representative example of how triplet exciton annihilators can be deployed as optically and electrically integrated interlayers to sensitize vertically-configured OPD and OSC device platforms via TTA reactions.

Results and discussion

Figure 1a presents the chemical structure of PtOEP, together with the frontier level alignment of the metallo-porphyrin with respect to the work function of the device electrodes. As shown in Figure 1b, the typical external quantum efficiency (EQE) spectrum of the PtOEP

View Article Online
DOI: 10.1039/D2TC00613E

photodiode confirms the responsivity to incoming light. A clear photo-response is observed, although the very low photocurrent generation efficiency of the system. In the EQE spectra, two spectral features are clearly discernible at 3.26 eV (380 nm) and at 2.25 eV (550 nm) with EQEs in the order of 0.10%. Direct comparison with the absorption spectrum of PtOEP in dilute solution points to the origin of the EQE features. The photocurrent peak detected at about 2.25 eV corresponds to onset of the Q-band in the absorption spectrum of PtOEP, thereby suggesting that charge photogeneration is barrierless. The high energy photocurrent peak is attributed to transitions within the Soret absorption band of PtOEP. With regard to the UV-vis absorption spectra in solution, both EQE features of PtOEP are spectrally broadened. Moreover, the full-width half maximum (FWHM) value of the photocurrent peak at 550 nm increases with respect to the FWHM value of the Q-absorption band. The low efficiency with which carriers are photogenerated in the PtOEP photodiode should not be surprising given the absence of a heterojunction in the photoactive layer that could drive exciton dissociation via charge transfer. One could argue that by considering the PtOEP layer thickness (120 nm) and the asymmetric electrodes used in the PtOEP-photodiode, the observed photocurrent originates from the portion of weakly bound PtOEP excitons that are fully separated by the build-in electric field of the photodiode device. Given the relatively low dielectric constant of PtOEP (ε=2.52), [47] the dissociation of the PtOEP excitons is likely facilitated by the well-ordered fraction of the thermally evaporated layer. [48] However, by recording the *J-V* characteristics of the PtOEP photodiodes under white light illumination, as provided by a Hg/Xe arc lamp, a different charge photogeneration mechanism is revealed.

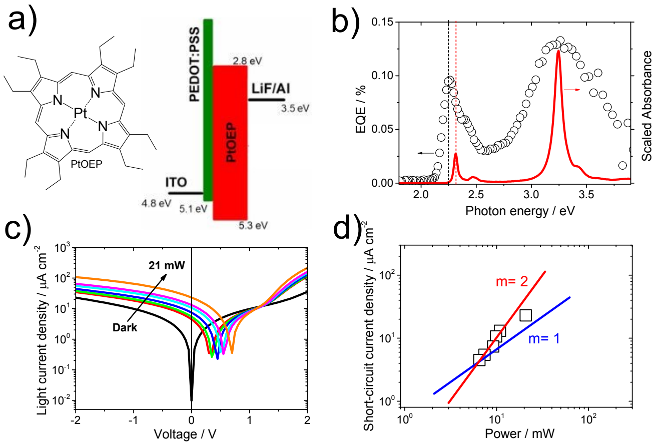

Figure 1: a) Chemical structure of PtOEP, energy levels of the materials and electrodes work function. b) the external quantum efficiency spectrum of a PtOEP device and the scaled absorption spectrum of a dilute PtOEP solution in toluene. The vertical dash lines correspond to the photocurrent peak at 2.25 eV (black) and to the Q-band absorption peak at 2.31 eV (red). c) *J-V* curves under dark and white-light illumination conditions. d) Logarithmic plot of the J_{SC} dependence on white-light illumination power. The solid lines correspond to a linear (blue line) and a quadratic (red line) dependence of J_{SC} on light power.

Figure 1c presents the obtained light *J-V* curves of the PtOEP diode at different incoming light powers, together with the dark *J-V* characteristics of the device. For an illumination power of 21 mW, the V_{OC} and J_{SC} of the device become 0.6 V and 23 μA cm^{-2}, respectively. Contrary to previous results of studies on the photoconductivity of porphyrin-based materials, [46, 49] Figure 1d shows that the device J_{SC} exhibits a quadratic dependence on photoexcitation. Considering the incoherent nature of light used for photoexciting the PtOEP device, this observation is rather surprising as it suggests the participation of a non-linear process [14, 15] in the mechanism of charge photogeneration in the single-component PtOEP device.

Unlike the case of cadmium sulfide, [50] metal chalcogenide [51, 52] and amorphous metal oxide photoconductors [53, 54] wherein two-center recombination processes result in a superlinear photoconductivity, the PtOEP photodiode exhibits a V_{OC} that requires the generation of free carriers through the activation of CT states. In addition, no heterojunction-type interfaces are present in the PtOEP device structure that can facilitate the accumulation of charges at the device electrodes. Charge accumulation may arise only due to the low charge carrier mobility in the PtOEP photoactive layer, which would manifest as a space charge limited (SCLC) photocurrent. SCLC effects are inferred by a sublinear dependence of the device photocurrent on optical power; that is a slope < 1 should be obtained in a double logarithmic plot [55] of the device J_{SC} on photoexcitation intensity. In contrast, the obtained quadratic J_{SC} dependence points towards a 'two-photon absorption'-like process that produces free carriers.

In order to gain solid insight on the observed photocurrent dependence on light power, we first addressed the structural properties of the PtOEP photoactive layer. Figure 2a presents the X-ray diffraction (XRD) pattern of a thermally evaporated PtOEP film on a quartz substrate. XRD diffractograms are also presented for PtOEP in the powder form and for a solution-processed PtOEP film, as the control samples. The latter was obtained by spin coating of a PtOEP solution in toluene in which PtOEP was mixed (10 wt%) with a high molecular weight poly(styrene) (PS) derivative.

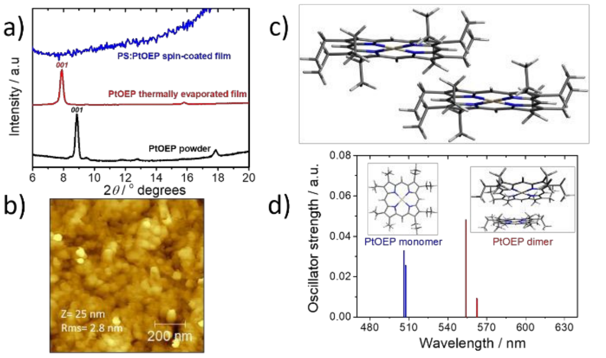

Figure 2. a) XRD patterns of the PtOEP system in the form of powder (black line), a thermally evaporated film (red line) and a spin-coated PS:PtOEP film (blue line). b) Tapping mode AFM image of the thermally evaporated PtOEP film on a glass/ITO/PEDOT:PSS electrode. c) DFT calculated side-view of the PtOEP dimer configuration, and d) oscillator strength for PtOEP monomer (blue) and dimer (red).

As shown in Figure 2a, the solution processed PS:PtOEP film is found to be amorphous. In contrast, the XRD pattern obtained from the thermally evaporated PtOEP film indicates the presence of PtOEP crystalline features that confirm the contribution of PtOEP structural order in photocurrent generation. With respect to the angular position of the (001) planes of PtOEP in the powder form PtOEP (2ϑ=

View Article Online
DOI: 10.1039/D2TC00662F

8.86°), the observed diffraction peak of the evaporated PtOEP film on quartz is placed at 2ϑ= 7.87°, indicating a periodicity of d= 11.2 Å. Control measurements on a similarly prepared PtOEP film evaporated on a glass/ITO/PEDOT:PSS electrode exhibited an identical XRD (not shown) without differences in the angular position of the PtOEP (001) planes, depicting that the underlying substrate (quartz or PEDOT:PSS) did not affect the crystallinity. The derived periodicity of 11.2 Å is attributed to the intercolumnar distance between PtOEP columns in the layer that adopt an edge-on orientation. [56] Based on the FWHM of the (001) diffraction peak the calculated coherence length of the PtOEP crystallite is L = 40 nm. We further applied atomic force microscopy (AFM) imaging for mapping the surface topography of the evaporated PtOEP film on glass/ITO/PEDOT:PSS substrate. As shown in Figure 2b the surface of the film is found smooth with a relatively low root mean square roughness (Rms= 2.8 nm). In good agreement with the obtained XRD characterization results, the topography mapping verifies the presence of agglomerates on the PtOEP film surface that are formed by spherical domains, with a sphere diameter ranging between 45 – 60 nm.

Both XRD and AFM studies provide evidence in support of the semicrystalline character of the thermally evaporated PtOEP film. To investigate the exciton coupling effects between the PtOEP molecules in the crystalline fraction of the film and address their impact on the absorption properties of the PtOEP system, density functional theory (DFT) calculations were performed on isolated (*i.e.* monomer) and aggregated (*i.e.* dimer) PtOEP species. The aggregation of PtOEP was studied based on constraint optimizations of the PtOEP dimer, wherein the interatomic Pt – Pt distance of the two π-π stacked PtOEP molecules was kept fixed to 8.165 Å, as obtained from the packing motif of the PtOEP single crystal. [57] In these calculations the ethyl side groups of the PtOEP macrocycle were explicitly considered. According to subsequent time-dependent DFT (TD-DFT) calculations the interaction of two PtOEP monomers affects the PtOEP Q-band spectral characteristics. As shown in Figure 2d, the low energy transitions found at 506 and 507 nm for the PtOEP monomer split and exhibit a red-shift to 554 nm and 562 nm for the constrained PtOEP dimer.

Furthermore, the UV-vis absorption spectrum of the thermally evaporated PtOEP film was measured. For reference purposes, the UV-vis spectrum of the spin-coated PS:PtOEP film was also recorded. Figure 3a and Figure 3b present the normalized absorption spectra of these films in the range 450 – 600 nm where the Q-band of the PtOEP film is positioned. The spectrum of the spin-coated PS:PtOEP is found similar to that of PtOEP in dilute solution (see Fig. 1b), exhibiting absorption peaks of the Q-bands at 503 nm and 537 nm. In contrast, the absorption spectrum of the thermally evaporated film is found distorted; the Q-bands are broadened and red-shifted, while a shoulder appears in the absorption band between 540 – 550 nm (see Figure S1 in ESI). In light of the TD-DFT findings, the splitting of the low energy Q-band is attributed to the onset of PtOEP dimer species formation in the thermally evaporated PtOEP film.

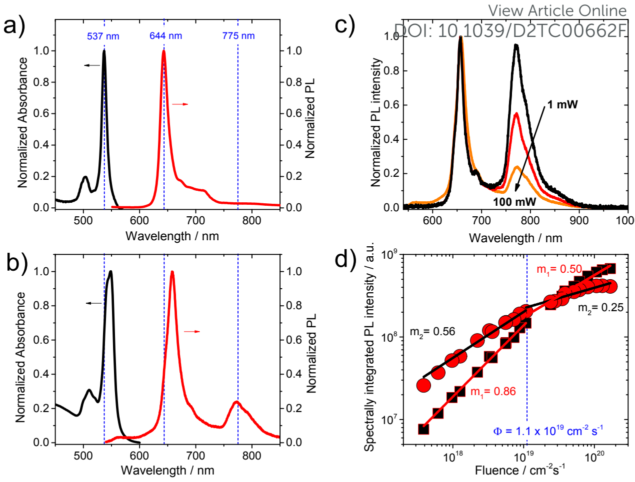

Figure 3. Normalized absorption (black line) and photoluminescence (red line) spectra of the a) spin-coated PS:PtOEP film and b) thermally evaporated PtOEP film. The vertical dash lines in (a) and (b) indicate the spectral positions at 537 nm, 644 nm and 775 nm. c) Normalized photoluminescence spectra of the thermally evaporated PtOEP film, as acquired at different laser photoexcitation powers; 1 mW (black line), 10 mW (red line) and 100 mW (orange line). d) The dependence of the spectrally integrated PL signal of the PtOEP monomer between 650 – 655 nm (squares) and the PtOEP dimer luminescence between 755 – 815 nm (circles) on laser fluence. The solid lines are power-law fits on the data, and the vertical dash line indicates the fluence at which a change in the exponent of the power law is observed (see main text). In all cases the data were acquired after CW laser photoexcitation at 532 nm.

Further evidence for the occurrence of intermolecular interactions comes from the comparison of the photoluminescence (PL) spectra of the spin-coated and thermally deposited PtOEP films, as obtained after photoexcitation at 532 nm. Comparing the PL spectra of the two systems, a red-shift is found in the typical PtOEP phosphorescence band, from 644 nm (PS:PtOEP, Figure 3a) to 650 nm (thermally evaporated PtOEP film, Figure 3b). Moreover, the characteristic signature of the triplet dimer PtOEP [58] is clearly detected in the PL spectrum of the thermally evaporated PtOEP film, positioned at 775 nm. Figure 3c presents the normalized PL spectra of the thermally evaporated film, as acquired after photoexcitation at 532 nm with progressively increased laser power. As laser power increases from 1 mW to 100 mW, the relative PL intensity of the PtOEP triplet dimer diminishes by exhibiting a ratiometric relationship with regard to the phosphorescence intensity of the PtOEP monomer. The dependence of the two PL spectral features on photoexcitation intensity was studied in more detail. Figure 3d presents the logarithmic plot of the fluence dependent spectrally integrated PL intensity (I_{PL}), for the signal of the monomeric PtOEP phosphorescence and of the PtOEP triplet dimer luminescence. For fluences up to 1×10^{19} cm^{-2} s^{-1} (~ 18.5 mW laser power), fitting both datasets with the power-law functional $I_{PL} \propto (\text{fluence})^m$ results in the power-law exponents m_1= 0.86 and m_2= 0.56, for the PtOEP monomer and for the PtOEP triplet dimer PL signals, respectively. The nearly square-root dependent intensity of the PtOEP triplet dimer emission on fluence suggests the occurrence of bimolecular annihilation events between the dimer species. Annihilation between CT states has been observed previously in other organic systems, [59] and similarly the PtOEP system in the form of thermally evaporated films is prone to these effects. [60] At the same photoexcitation regime, the dependence of the PtOEP monomer phosphorescence is nearly linear, and only when fluences higher than 1×10^{19} cm^{-2} s^{-1} are used, a square-root dependence is observed that suggests the onset of TTA reactions between triplet PtOEP excitons in the evaporated PtOEP film. The different thresholds of fluence where TTA reactions become important for the PtOEP triplet exciton and the PtOEP triplet dimer relate to their diffusion coefficient. [61] With respect to the triplet PtOEP excitons, the triplet PtOEP dimer species is more susceptible to bimolecular reactions due to its lower diffusion coefficient. [60] Interestingly, the bimolecular annihilation effects between triplet PtOEP dimer species correlate with the non-linear photocurrent generation processes shown in Fig.1d. Considering the PL band of the triplet PtOEP dimer at 775 nm, the energy reached by dimer annihilation is placed at 3.2 eV, which is isoenergetic with the higher-lying PtOEP energy level responsible for the Soret absorption band. The exciton binding energy at higher-lying states is reduced, thereby enabling the activation of the CT manifold. [12, 62] In the ideal case where the formation of PtOEP dimers was suppressed, fusion of two PtOEP triplet excitons in a solid-state environment would also hold the potential to drive CT activation. However, apart from the energetics, spin statistics should also be considered for evaluating the coupling of the spatially separated (T…T) pair [63] with the CT states. Future attempts to develop dimer-free PtOEP films could rely on the chemical modification of PtOEP *i.e.* by the attachment of bulky substituents on the porphyrin macrocycle that would hinder close π-π stacking.

In order to understand better how the fusion events between PtOEP triplet dimer photoexcited states impact the photo-response of the PtOEP photodiodes, *J-V* characteristics were recorded for a range of 532 nm laser photoexcitation intensities.

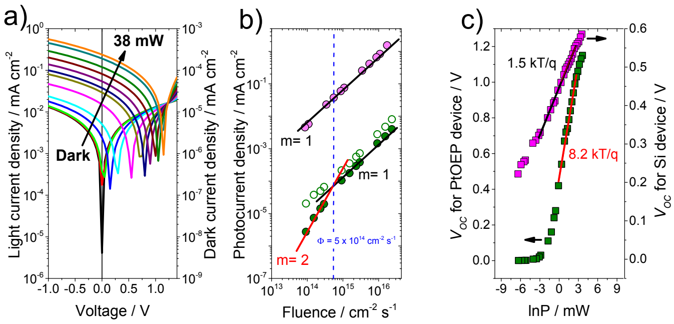

Figure 4. a) *J-V* curves of PtOEP device under 532 nm cw laser photoexcitation. The dark current *J-V* curve of the device is also presented. b) PtOEP-photodiode short-circuit current density (green solid circles) and photocurrent density at -1 V (green open circles) dependence on laser fluence. The J_{SC} dependence of a reference Si-based photodiode (magenta solid circles) is also displayed. The solid lines correspond to a linear (black line) and a quadratic (red line) dependence of photocurrent density on fluence. The vertical dash line indicates the fluence at which a change in the exponent of the power law is observed. c) Open-circuit voltage (V_{OC}) as a function of the natural logarithm of excitation laser power (lnP) for the PtOEP-based (green squares) and the Si-based (magenta squares) photodiodes. Solid lines are fit on the data (see main text).

The *J-V* curves acquired at different laser powers are presented in Fig. 4a, together with the corresponding dark *J-V* curve of the PtOEP-based device. From the data shown in Fig. 4a, the J_{SC} and V_{OC} parameters of the PtOEP device were derived for each laser power. For reference purposes, a commercially available silicon (Si)-based photodetector (SM05PD1A, Thorlabs) was characterized under identical photoexcitation conditions.

View Article Online
DOI: 10.1039/D2TC00662F

Figure 4b presents the dependence of J_{SC} on laser fluence in a logarithmic plot. In good agreement with the trend seen in Fig. 1d, a supralinear dependence of J_{SC} on laser fluence is observed. For fluences lower than 5.48×10^{14} cm^{-2}s^{-1} (~ 18 µW average laser power) the J_{SC} dependence on fluence is nearly quadratic, whereas at higher fluences it becomes linear. This square-to-linear transition is not observed in the case of the reference Si-based photodetector, which exhibits a linear response across the entire fluence range used. When operating the PtOEP device at a -1 V reverse bias, the dependence of photocurrent density J_{Ph} on fluence becomes linear across the whole fluence regime. In the presence of an externally applied electric field, the photogenerated charges become more mobile and they have an increased probability to participate in annihilation reactions with the PtOEP triplet excited states. [64] Triplet – charge annihilation effects are known to have an antagonistic relationship with the TTA process in photoactive layers of organic LEDs [65] and they are also operative in organic PV devices. [66]

Another factor that would impact negatively on the photoresponse of the PtOEP device is the presence of molecular oxygen that would quench quantitatively the triplet excited state of PtOEP. [67] For our study, oxygen-effects were mitigated via the thorough encapsulation of the PtOEP photodiodes in an inert atmosphere. In contrast, a previous study [46] that monitored the fluence-dependent photocurrent of non-encapsulated PtOEP photodiodes in ambient, did not register a quadratic photocurrent response on light intensity. Since those devices involved thermally evaporated PtOEP layers that also contained the PtOEP dimer species, we suggest with caution that the quadratic response was masked by oxygen-induced quenching effects of the PtOEP triplets.

Drawing attention to the impact of increasing photoexcitation intensity on V_{OC}, Figure 4c presents the dependence of the device V_{OC} on laser power. The V_{OC} of the PtOEP-only device gradually rises as laser power increases reaching to a plateau of 1.15 V. In principle, the dependence of V_{OC} on excitation intensity is expressed according to $V_{OC} = \beta\frac{kT}{q}\ln P$, where k corresponds to the Boltzmann constant, T to the absolute temperature, β to the thermal voltage ($\frac{kT}{q}$) coefficient, and P to the laser power. [68] When fitting in this manner, the thermal voltage coefficient value of β= 8 is obtained. This is well above the typical values expected between 1 and 2 and it indicates a non-optimized PtOEP photoactive layer microstructure wherein severe non-geminate recombination losses are operative. [69] Instead, for the reference Si-photodiode a thermal voltage coefficient of β= 1.5 is found. Abnormal values of the thermal voltage coefficient are frequently obtained in fullerene-free organic solar cell devices, developed by disk-shaped perylene diimide electron acceptors that pack closely to form charge carrier trapping sites. [70] Similarly, the performance of the PtOEP-only device is limited primarily by the improper edge-on orientation arrangement of the disk-shaped PtOEP molecules on the device electrodes. This packing motif places the PtOEP π-π stacking direction orthogonally with respect to the required charge flow paths across the device electrodes. The structural defects that arise from the edge-on oriented π-π stacking of PtOEP impact negatively on charge transport and charge extraction. Indeed, severe charge recombination losses are inferred by the dependence fill factor of the PtOEP device on laser fluence (see Figure S2 in ESI). Additionally, based on the dark *J-V* curves of

View Article Online
DOI: 10.1039/D2TC00662F

unipolar hole-only PtOEP devices (see Figure S3 in ESI), the zero-field hole (μ_h) mobility was determined to be $\mu_h = 1.7 \times 10^{-11}$ cm^2 V^{-1} s^{-1}.

Despite the non-optimized microstructure of the thermally evaporated PtOEP layer, the PtOEP-based photodiode offers an ideal opportunity to establish an ultrasensitive photodetection platform that operates based on supralinear photocurrent generation under low photoexcitation power. Figure 5 presents the power-dependent values of the photodiode responsivity, *R*. At -1 V reverse bias *R* is virtually independent on fluence, following the $R \propto$ fluence$^{0.007}$ power-law. Practically it is found that *R* remains close to the level of 0.8 mA W^{-1}, while J_d is 13.2 µA cm^{-2}. In comparison with the state-of-the-art OPDs, the significantly weaker responsivity of the herein presented PtOEP-based photodetector is not surprising, considering that no second component is present in the PtOEP active layer to drive exciton dissociation. Instead, the observed square-root dependence of the PtOEP triplet dimer luminescence on fluence suggests that charge photogeneration in the single-component PtOEP active layer is driven by TTA reactions. Contrary to the conventional route for charge photogeneration via the dissociation of excitons formed by one-photon electronic transitions, the TTA-driven charge generation mechanism in the single component PtOEP layer is less efficient due to its bimolecular nature. The applicability of the PtOEP system as a TTA-operated OPD unit was examined further by considering the *NEP* and D^* figures of merit. As presented in Table 1, the high J_d and low *R* values of the PtOEP photodetector concomitantly result in *NEP* and D^* values within 0.4 – 0.9 nW Hz$^{-1/2}$ and 2.5 – 6 × 10^8 Jones, respectively. Table 1 summarizes the values of these parameters when operating the PtOEP- photodiode at the reverse bias of -1 V and -0.5 V, under 532 nm CW laser illumination within the 1 µW – 3 mW regime of optical excitation.

	Photodetector at -1 V operation		*Photodetector at -0.5 V operation*	
Light power / µW	NEP_{-1V} / pW Hz$^{-1/2}$ $^{(a)}$	D^*_{-1V} / Jones	$NEP_{-0.5V}$ / pW Hz$^{-1/2}$ $^{(a)}$	$D^*_{-0.5V}$ / Jones
1.8	790	2.91×10^8	904	2.53×10^8
3	710	3.24×10^8	799	2.87×10^8
4.6	820	2.78×10^8	875	2.62×10^8
5.8	780	2.93×10^8	860	2.66×10^8
30	760	3.00×10^8	705	3.25×10^8
300	570	4.05×10^8	518	4.42×10^8
920	400	5.77×10^8	380	6.03×10^8
2910	390	5.92×10^8	384	5.97×10^8

Table 1: Optical power dependent values of the noise equivalent power (*NEP*) and specific detectivity (*D**) parameters for the PtOEP photodiode operated at -1 V and at -0.5 V reverse bias, under 532 nm laser CW-excitation. $^{(a)}$ as measured at 1 Hz.

The benefit of employing the non-linear photoresponse of the PtOEP photodiode in photodetection applications becomes clearer when operating the device at short-circuit. In this case, in comparison with conventional OPDs, the PtOEP system offers the competitive advantage of high sensitivity to low power optical stimulation signals of a narrow spectral range. As shown in Figure 5, a gradual increase is observed in *R* for fluences below 10^{15} cm^{-2} s^{-1} and the power-law dependence of $R \propto$ fluence$^{0.560}$ is obtained. At short-circuit conditions, J_d is vanishing and the detectivity of the PtOEP photodiode is inherently limited by thermal noise. [18] Converting the obtained responsivity to EQE at 532 nm (EQE$_{532\ nm}$) rules out the contribution of gain effects that could possibly arise from a photoconductive-like response of the PtOEP-only device. In respect to short-circuit conditions, the EQE$_{532\ nm}$ at -1V device operation increases only by a factor of 7 (see Figure S4 in ESI). The large differences in the responsivity of the PtOEP photodiode on minute differences in the incoming low-level photoexcitation intensity establishes this system as an ulstrasensitive light probe tool. The highly selective and ultrasensitive photodetecting response of the PtOEP photodiode within the 500 – 560 nm narrow spectral range is an attribute that can be utilized in next generation photonic and biophotonic applications. [14, 27]

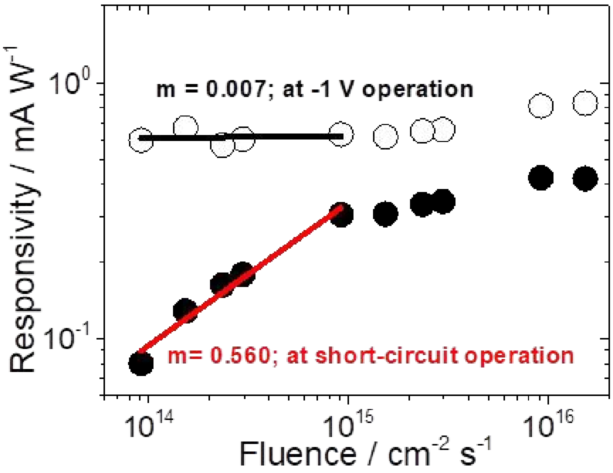

Figure 5. Fluence dependent responsivity of the PtOEP device when operating at short-circuit (filled symbols) and -1 V (open symbols) reverse bias conditions under illumination with a CW 532 nm laser. Solid lines correspond to fits on the data as obtained based on the $R \propto$ Fluence^m power-law.

Experimental

Materials

Poly(styrene) (PS, average M$_w$=192 kDa) was purchased from Sigma-Aldrich, poly(3,4-ethylenedioxythiophene) polystyrene sulfonate (PEDOT:PSS) was purchased from Merck (Clevios HTL Solar) and PtOEP was purchased from Frontier Scientific Inc. All materials were used as received without further purification.

Solution-processing and film development

Binary films of PS:PtOEP 10 wt% were deposited via spin coating of degassed solutions in toluene (10 mg/ml vs. PS) onto fused silica quartz substrates, in a nitrogen-filled glovebox. Spin-coating was performed at 3000 rpm for 1 min and prior to their removal from the glovebox the obtained films were thermally annealed at 70°C for 10 min.

Deposition of PtOEP film and fabrication of PtOEP-only device

Thermally evaporated PtOEP films were developed on fused silica substrates. Photodiode devices with thermally evaporated PtOEP active layers were developed based on the conventional device configuration of glass/indium tin oxide (ITO)/ PEDOT:PSS/PtOEP/lithium fluoride (LiF)/Aluminum (Al). The glass/ITO electrodes (XY15S, ITO substrates from Xin Yan Technology Ltd.) were ultrasonically cleaned using acetone and isopropanol for 15 min. After preliminary cleaning, the substrates were washed with Hellmanex III to remove contaminants and residues from the ITO surface. The substrates were again cleaned with deionized water followed by acetone and isopropanol for 15 min and soon after being placed in oxygen plasma (100 W power) for 10 min. A solution-processed hole-collecting interlayer of PEDOT:PSS was spin-coated at 3000 rpm for 1 min onto the ITO electrodes and thermal annealing was applied at 200 ^{o}C for 20 minutes. The glass/ITO/PEDOT:PSS electrodes were transferred in a N_2-filled glovebox (PureLabHE, Inert) and a thermal evaporator (Covap III, Angstrom Engineering Inc.) coupled to the N_2-filled glovebox was used for depositing PtOEP in vacuum (4×10^{-8} mbar) at a rate of 0.5 Å/s. A shadow mask was used for facilitating the formation of a PtOEP layer area of 0.8 cm^2. The thickness of the obtained PtOEP film was 120 nm, as determined by a Tencor P16 Stylus profiler. The device structure was completed with the deposition of thermally evaporated LiF interlayer (~2 nm) at a rate of 0.1 Å/s capped by an Al (160 nm) metal electrode. A shadow mask facilitated the LiF interlayer and metal electrode deposition so that an effective device area of 0.0525 cm^2 was finally obtained. Prior to their removal from the glovebox the glass/ITO/PEDOT:PSS/PtOEP/LiF/Al photodiodes were encapsulated with glass slides and epoxy resin.

UV-vis absorption

The absorption spectra of the thermally evaporated PtOEP and the PS:PtOEP films were recorded with a UV-2700 Shimadzu spectrophotometer operated in transmission mode. In all cases, a spectral band width of 1 nm and a scan rate of 1 nm/s were used. For measuring the absorption spectra of the PtOEP solution in toluene, a cuvette of 10 mm path length was used and the obtained spectrum was corrected with respect to the absorption spectrum of pure toluene.

Photoluminescence spectroscopy

Time-integrated photoluminescence (PL) spectra of the PtOEP films deposited on quartz fused silica substrates were recorded at room temperature after excitation of the films with the 532 nm line of a DPSS CW laser (MGL-III-532, CNI Optoelectronics Tech.CO. Ltd). The emitted light was dispersed in a mini spectrograph (FLAME-S-VIS-NIR-ES, Ocean Insight) and detected with a Sony ILX511B linear silicon CCD array. During PL characterization the films were kept in a cryostat that was evacuated by a turbomolecular pump (HighCube 80 Dry Vacuum Pumping Station, Pfeiffer Vacuum) so that a dynamic vacuum of a typical pressure of 10^{-6} mbar was maintained during the measurements. Photoexcitation intensity-dependent measurements were performed by using the combination of a set of neutral density filters of known transmittance values at 532 nm and the average laser power was determined with a thermopile power sensor (PS19Q, Coherent Inc.) coupled to a FieldMaxII-TOP power/energy meter (Coherent Inc.).

Atomic force microscopy imaging

AFM imaging was performed with a Dimension Icon Bruker AFM microscope operated in a tapping mode and triangular geometry probes (Scanasyst-Air) with a nominal tip radius of 2 nm (max. 12 nm) were used. Topography mapping of the PtOEP thin films was applied on thermally evaporated PtOEP layers deposited on glass/ITO/PEDOT:PSS substrates. Image processing and statistical analysis were conducted using the Gwyddion software.

X-ray diffraction

The x-ray diffraction (XRD) patterns were acquired in an Ultima IV (Rigaku) diffractometer, equipped with a Cu tube (Cu Kα, $\lambda = 0.15418$ nm) and operated at 40 kV and 40 mA. The x-ray beam of the instrument was configured in parallel mode by a multilayer curved mirror optics (CBO) and the patterns were acquired in conventional Bragg-Brentano scans in the 2ϑ range of 5 – 20 ^{o}.

External Quantum Efficiency and light J-V

External quantum efficiency (EQE) spectra were registered after the monochromatic illumination of the photodiodes by a 250 W power Quartz Tungsten Halogen (QTH) lamp enclosed in an F/1-aperture lamp housing and coupled to a Cornerstone 1/8 m monochromator (CS-130-USB-3-MC, Newport), capable of covering the 300-2200 nm spectral range. The optical power output of the lamp was determined based on a calibrating photodiode (818-UV/DB UV Detector, Newport DB15 Calibration Module) with known responsivity, and the EQE spectra of the devices were determined based on the device photocurrent as acquired by a source meter unit (SMU 2401, Keithley) with a detection limit of 10 pA (corresponding to 190 pA/cm^2 considering the effective area of the devices under test) and 1 µV. Photocurrent density – voltage characteristics of the PtOEP photodiodes were registered both under white light illumination and after laser photoexcitation. A Hg/Xe light source (Research F/2.2 Illumination Source 200 W Hg/Xe Ozone-free Arc Lamp, Newport) was used as the white light source, the output of which was determined based on a calibrating photodiode. For laser induced photocurrent measurements a DPSS CW 532 nm laser (MGL-III-532, CNI Optoelectronics Tech.CO. Ltd) was used. The acquired light *J-V* curves were registered as the output of the Hg/Xe light source and the CW laser were attenuated progressively with neutral density filters of known transmittance. Subtraction of the dark current density from the light current density values resulted in the photocurrent density values for each light illumination intensity.

Dark Current Characterization

The dark current density of all photodiodes was monitored with the acquisition of dark *J-V* curves recorded in the voltage range between -2 and 3 V when a Keithley electrometer (SMU 2401) was used. Unipolar hole-only devices with thermally evaporated PtOEP layers were fabricated for studying charge transport properties of the PtOEP system. The device configuration of the hole-only was glass/ITO/PEDOT:PSS/PtOEP/Au. The thickness of thermally evaporated PtOEP films was determined by a Tencor P16 Stylus profiler.

Density functional theory (DFT) calculations

A number of exchange-correlation functionals (CAM-B3LYP, PBE1PBE, M06-L, M06-2X, MN12-L, M11-L) were tested, however M11-L was chosen due to its good performance in organometallics. The M11-L functional provides a very good description of the energetics for singlet and triplet excited states (both for absorption and emission) in comparison to experiment for PtOEP and similar Pt-containing porphyrin compounds. The ground state equilibrium geometries of monomer and dimer PtOEP species were obtained through DFT using the dual-range local exchange-correlation functional M11-L and a mixed basis set, the triple-ζ Pople 6-311++G(d,p) basis set for C, H and N atoms and a Lanl2DZ basis with effective core potential for Pt. Vertical excited state energies were computed with linear response time-dependent DFT on the basis of the optimized ground structures using the same functional and basis set. All calculations were performed using the Gaussian 16 software package. [71]

Conclusions

In summary, we studied the electro-optical properties of a single-component organic photodetector with a thermally evaporated PtOEP photoactive layer. Owing to the crystalline character of the PtOEP absorber, triplet dimer PtOEP species are formed in the layer that are prone to optically induced annihilation effects. With these structural characteristics, in addition to the role of light absorber, the PtOEP photoactive layer serves also as an electrically-integrated self-TTA activator and charge transporter in the device structure. The annihilation of triplet dimer PtOEP species in the layer of the PtOEP-only photodiode correlates with the process of charge photogeneration under low power illumination, and in combination with the deep HOMO level of PtOEP the development of a V_{OC} as high as 1.15 V was achieved. In light of the observed supralinear J_{SC} dependence on photoexcitation intensity, the bimolecular annihilation effects between triplet PtOEP dimers are proposed as the mechanism responsible for the generation of photocurrent in the single-component PtOEP photodiode. Apart from gaining deeper insight in the processes of free charge carrier formation in organic materials, the presented PtOEP-based device structure holds promise for the generic sensitization of organic and hybrid solar cells with vertical device configuration. [64] Moreover, the capability of PtOEP to activate photocurrent via self-TTA reactions is an added value to be utilized by a manifold of smart light-management photonic devices. A broad gamut of applications is envisioned including the use of TTA interlayers for sensitizing visible-blind photodetecting devices, [72] stimulating neuromorphic [73] and light-gated neural circuitries, [74] and augmenting light-driven photocatalytic tandem platforms. [75] The realization of those device architectures would be simplified greatly by the deposition of TTA interlayers via solution processing techniques. Alignment of the π-π stacking direction in the TTA interlayers with the device electrode directionality could be achieved if surface modification agents [76] were introduced for driving the growth of PtOEP columnar structures in a face-on arrangement. Towards this route, care should be taken so that the TTA interlayers will maintain the role of the charge collecting component in the device structure, without creating interfacial barriers that could potentially impede charge extraction. This can be ensured by tuning the frontier orbital energy of the triplet emitters via careful material design and tailored chemical modification of the molecular structure.

Author Contributions

GN developed the PtOEP layers and investigated their spectroscopic properties. PY established the methodology for device fabrication and engineering. GN and PY fabricated the OPD devices and GN investigated their optoelectronic properties. PY was in charge of developing all computer code and supporting algorithms that facilitated the coupling and the handling of the electro-optical equipment. LK investigated the structural properties of the PtOEP layers. DF and SA were in charge of the DFT calculations. DGG, JP and TP investigated the morphology of the device layers and determined their thickness. GN, PEK, PY, LK, JP and DGG performed the formal analysis of the experimental data. PEK conceived the project, conceptualized the work, supervised the overall research activity and was in charge of the funding acquisition from Research and Innovation Foundation. PEK wrote the manuscript with the contribution from all authors and revised its final version. All authors have given approval to the final version of the manuscript.

Conflicts of interest

View Article Online
DOI: 10.1039/D2TC00662F

There are no conflicts to declare.

Acknowledgements

This work was co-funded by the European Regional Development Fund and the Republic of Cyprus through project EXCELLENCE/1216/0010 ‘Low Photon-Energy Up-Conversion induced Sensitized Photocurrent Generation in Organic Photodiodes’ of the Research and Innovation Foundation, and was supported by Comunidad de Madrid (Spain) - multiannual agreement with UC3M (“Excelencia para el Profesorado Universitario” - EPUC3M14) - Fifth regional research plan 2016-2020 and by the Spanish Ministry of Science, Innovation and Universities (MICINN) through project RTI2018-101020-B-100.

Notes and references

1. G. Hong, X. Gan, C. Leonhardt, Z. Zhang, J. Seibert, J. M. Busch and S. Bräse, *Advanced Materials*, 2021, **33**, 2005630.
2. A. F. Paterson, S. Singh, K. J. Fallon, T. Hodsden, Y. Han, B. C. Schroeder, H. Bronstein, M. Heeney, I. McCulloch and T. D. Anthopoulos, *Advanced Materials*, 2018, **30**, 1801079.
3. L. X. Chen, *ACS Energy Letters*, 2019, **4**, 2537-2539.
4. H. Ren, J.-D. Chen, Y.-Q. Li and J.-X. Tang, *Advanced Science*, 2021, **8**, 2002418.
5. E. A. Silinsh, V. A. Kolesnikov, I. J. Muzikante and D. R. Balode, *Phys. Stat. Sol. B*, 1982, **113**, 379-393.
6. A. J. Heeger, *Advanced Materials*, 2014, **26**, 10-28.
7. S. Athanasopoulos, F. Schauer, V. Nádaždy, M. Weiß, F.-J. Kahle, U. Scherf, H. Bässler and A. Köhler, *Advanced Energy Materials*, 2019, **9**, 1900814.
8. K. Vandewal, S. Albrecht, E. T. Hoke, K. R. Graham, J. Widmer, J. D. Douglas, M. Schubert, W. R. Mateker, J. T. Bloking, G. F. Burkhard, A. Sellinger, J. M. J. Fréchet, A. Amassian, M. K. Riede, M. D. McGehee, D. Neher and A. Salleo, *Nature Materials*, 2014, **13**, 63-68.
9. V. Gulbinas, D. Hertel, A. Yartsev and V. Sundström, *Physical Review B*, 2007, **76**, 235203.
10. T. M. Clarke and J. R. Durrant, *Chemical Reviews*, 2010, **110**, 6736-6767.
11. R. Kersting, U. Lemmer, M. Deussen, H. J. Bakker, R. F. Mahrt, H. Kurz, V. I. Arkhipov, H. Bässler and E. O. Göbel, *Physical Review Letters*, 1994, **73**, 1440-1443.
12. T. Hahn, S. Tscheuschner, C. Saller, P. Strohriegl, P. Boregowda, T. Mukhopadhyay, S. Patil, D. Neher, H. Bässler and A. Köhler, *The Journal of Physical Chemistry C*, 2016, **120**, 25083-25091.
13. Y. Dong, V. C. Nikolis, F. Talnack, Y.-C. Chin, J. Benduhn, G. Londi, J. Kublitski, X. Zheng, S. C. B. Mannsfeld, D. Spoltore, L. Muccioli, J. Li, X. Blase, D. Beljonne, J.-S. Kim, A. A. Bakulin, G. D’Avino, J. R. Durrant and K. Vandewal, *Nature Communications*, 2020, **11**, 4617.
14. R. Koeppe, J. G. Müller, J. M. Lupton, J. Feldmann, U. Scherf and U. Lemmer, *Appl. Phys. Lett.* , 2003, **82**, 2601-2603.
15. M. Garbugli, A. Gambetta, S. Schrader, T. Virgili and G. Lanzani, *Journal of Materials Chemistry*, 2009, **19**, 7551-7560.

View Article Online
DOI: 10.1039/D2TC00662F

16. K.-J. Baeg, M. Binda, D. Natali, M. Caironi and Y.-Y. Noh, *Advanced Materials*, 2013, **25**, 4267-4295.
17. R. D. Jansen-van Vuuren, A. Armin, A. K. Pandey, P. L. Burn and P. Meredith, *Advanced Materials*, 2016, **28**, 4766-4802.
18. D. Yang and D. Ma, *Advanced Optical Materials*, 2019, **7**, 1800522.
19. X. Gong, M. Tong, Y. Xia, W. Cai, J. S. Moon, Y. Cao, G. Yu, C. L. Shieh, B. Nilsson and A. J. Heeger, *Science*, 2009, **325**, 1665-1667.
20. H. Bristow, P. Jacoutot, A. D. Scaccabarozzi, M. Babics, M. Moser, A. Wadsworth, T. D. Anthopoulos, A. Bakulin, I. McCulloch and N. Gasparini, *ACS Applied Materials & Interfaces*, 2020, **12**, 48836-48844.
21. I. K. Kim, J. H. Jo, J. Lee and Y. J. Choi, *Organic Electronics*, 2018, **57**, 89-92.
22. M. Ramuz, L. Bürgi, C. Winnewisser and P. Seitz, *Organic Electronics*, 2008, **9**, 369-376.
23. D. G. Georgiadou, Y.-H. Lin, J. Lim, S. Ratnasingham, M. A. McLachlan, H. J. Snaith and T. D. Anthopoulos, *Advanced Functional Materials*, 2019, **29**, 1901371.
24. K.-H. Lee, D.-S. Leem, J. S. Castrucci, K.-B. Park, X. Bulliard, K.-S. Kim, Y. W. Jin, S. Lee, T. P. Bender and S. Y. Park, *ACS Applied Materials & Interfaces*, 2013, **5**, 13089-13095.
25. S. F. Tedde, J. Kern, T. Sterzl, J. Fürst, P. Lugli and O. Hayden, *Nano Letters*, 2009, **9**, 980-983.
26. R. K. Canjeevaram Balasubramanyam, A. E. Kandjani, C. J. Harrison, S. S. A. Abdul Haroon Rashid, Y. M. Sabri, S. K. Bhargava, R. Narayan, P. Basak and S. J. Ippolito, *ACS Applied Materials & Interfaces*, 2017, **9**, 27875-27882.
27. J. Clark and G. Lanzani, *Nature Photonics*, 2010, **4**, 438-446.
28. E. Fron, G. Schweitzer, J. Jacob , A. Van Vooren, D. Beljonne, K. Müllen, J. Hofkens, M. Van der Auweraer and F. C. De Schryver, *ChemPhysChem*, 2007, **8**, 1386-1393.
29. I. G. Scheblykin, A. Yartsev, T. Pullerits, V. Gulbinas and V. Sundström, *The Journal of Physical Chemistry B*, 2007, **111**, 6303-6321.
30. D. W. Gehrig, I. A. Howard and F. Laquai, *The Journal of Physical Chemistry C*, 2015, **119**, 13509-13515.
31. M. A. Baldo, D. F. O'Brien, Y. You, A. Shoustikov, S. Sibley, M. E. Thompson and S. R. Forrest, *Nature*, 1998, **395**, 151-154.
32. A. K. Bansal, W. Holzer, A. Penzkofer and T. Tsuboi, *Chemical Physics*, 2006, **330**, 118-129.
33. F. Nifiatis, W. Su, J. E. Haley, J. E. Slagle and T. M. Cooper, *The Journal of Physical Chemistry A*, 2011, **115**, 13764-13772.
34. T. Tsuboi, M. Tanigawa, S. Kawami and T. Tsuji, *Current Applied Physics*, 2005, **5**, 633-639.
35. X.-H. Yang, F. Jaiser and D. Neher, in *Highly Efficient OLEDs with Phosphorescent Materials*, 2007, DOI: https://doi.org/10.1002/9783527621309.ch6, pp. 221-258.
36. P. E. Keivanidis, S. Baluschev, T. Miteva, G. Nelles, U. Scherf, A. Yasuda and G. Wegner, *Advanced Materials*, 2003, **15**, 2095-2098.
37. S. Baluschev, P. E. Keivanidis, G. Wegner, J. Jacob, A. C. Grimsdale, K. Müllen, T. Miteva, A. Yasuda and G. Nelles, *Appl. Phys. Lett.*, 2005, **86**, 061904.
38. P. E. Keivanidis, S. Baluschev, G. Lieser and G. Wegner, *ChemPhysChem*, 2009, **10**, 2316-2326.
39. P. E. Keivanidis, F. Laquai, J. W. F. Robertson, S. Baluschev, J. Jacob, K. Müllen and G. Wegner, *J. Phys. Chem. Lett.*, 2011, **2**, 1893-1899.
40. J. A. Hinke, T. J. Pundsack, W. A. Luhman, R. J. Holmes and D. A. Blank, *J. Chem. Phys.*, 2013, **139**, 101102.
41. H. Goudarzi, S. Limbu, J. Cabanillas-González, V. M. Zenonos, J.-S. Kim and P. E. Keivanidis, *Journal of Materials Chemistry C*, 2019, **7**, 3634-3643.
42. Y.-Y. Noh, J.-J. Kim, Y. Yoshida and K. Yase, *Advanced Materials*, 2003, **15**, 699-702.
43. T. J. Savenije and A. Goossens, *Physical Review B*, 2001, **64**, 115323.
44. M. Campione, E. Fumagalli, L. Raimondo, A. Monguzzi, F. Meinardi and A. Sassella, *Chem. Matter.*, 2011, **23**, 832-840.
45. M. D. Perez, C. Borek, P. I. Djurovich, E. I. Mayo, R. R. Lunt, S. R. Forrest and M. E. Thompson, *Advanced Materials*, 2009, **21**, 1517-1520.
46. J. Kalinowski, W. Stampor, J. Szmytkowski, M. Cocchi, D. Virgili, V. Fattori and P. D. Marco, *The Journal of Chemical Physics*, 2005, **122**, 154710.
47. A. A. Abuelwafa, A. El-Denglawey, M. Dongol, M. M. El-Nahass and T. Soga, *Journal of Alloys and Compounds*, 2016, **655**, 415-422.
48. S. Gélinas, A. Rao, A. Kumar, S. L. Smith, A. W. Chin, J. Clark, T. S. v. d. Poll, G. C. Bazan and R. H. Friend, *Science*, 2014, **343**, 512-516.
49. B. Borders, M. Adinehnia, N. Rosenkrantz, M. v. Zijll, K. W. Hipps and U. Mazur, *Journal of Porphyrins and Phthalocyanines*, 2017, **21**, 569-580.
50. R. H. Bube, *Journal of Physics and Chemistry of Solids*, 1957, **1**, 234-248.
51. J. A. Peters, N. K. Cho, Z. Liu, B. W. Wessels, H. Li, J. Androulakis and M. G. Kanatzidis, *Journal of Applied Physics*, 2012, **112**, 063702.
52. V. Klee, E. Preciado, D. Barroso, A. E. Nguyen, C. Lee, K. J. Erickson, M. Triplett, B. Davis, I. H. Lu, S. Bobek, J. McKinley, J. P. Martinez, J. Mann, A. A. Talin, L. Bartels and F. Léonard, *Nano Letters*, 2015, **15**, 2612-2619.
53. C.-Y. Nam and A. Stein, *Advanced Optical Materials*, 2017, **5**, 1770119.
54. H. Lu, X. Zhou, T. Liang, L. Zhang and S. Zhang, *Appl. Phys. Lett.*, 2018, **112**, 042103.
55. L. J. A. Koster, V. D. Mihailetchi, H. Xie and P. W. M. Blom, *Appl. Phys. Lett.*, 2005, **87**, 203502.
56. C.-M. Che, H.-F. Xiang, S. S.-Y. Chui, Z.-X. Xu, V. A. L. Roy, J. J. Yan, W.-F. Fu, P. T. Lai and I. D. Williams, *Chemistry – An Asian Journal*, 2008, **3**, 1092-1103.
57. L. R. Milgrom, R. N. Sheppard, A. M. Z. Slawin and D. J. Williams, *Polyhedron*, 1988, **7**, 57-61.
58. T. Dienel, H. Proehl, T. Fritz and K. Leo, *Journal of Luminescence*, 2004, **110**, 253-257.
59. T. D. M. Bell, J. Jacob, M. Angeles-Izquierdo, E. Fron, F. Nolde, J. Hofkens, K. Müllen and F. C. D. Schryver, *Chemical Communications*, 2005, DOI: 10.1039/B509651K, 4973-4975.
60. J. Mężyk, J. Kalinowski, F. Meinardi and R. Tubino, *Applied Physics Letters*, 2005, **86**, 111916.
61. R. Saxena, T. Meier, S. Athanasopoulos, H. Bässler and A. Köhler, *Physical Review Applied*, 2020, **14**, 034050.
62. B. Minaev, E. Jansson, H. Ågren and S. Schrader, *J. Chem. Phys.*, 2006, **125**, 234704.

View Article Online
DOI: 10.1039/D2TC00662F

63. A. J. Musser and J. Clark, *Annu. Rev. Phys. Chem.*, 2019, **70**, 323-351.
64. Y. L. Lin, M. Koch, A. N. Brigeman, D. M. E. Freeman, L. Zhao, H. Bronstein, N. C. Giebink, G. D. Scholes and B. P. Rand, *Energy & Environmental Science*, 2017, **10**, 1465-1475.
65. H. v. Eersel, P. A. Bobbert, R. A. J. Janssen and R. Coehoorn, *J. Appl. Phys.*, 2016, **119**, 163102.
66. J. M. Marin-Beloqui, D. T. W. Toolan, N. A. Panjwani, S. Limbu, J.-S. Kim and T. M. Clarke, *Adv. Ener. Mater.*, 2021, **11**, 2100539.
67. E. Aluicio-Sarduy, A. Baidak, G. C. Vougioukalakis and P. E. Keivanidis, *The Journal of Physical Chemistry C*, 2014, **118**, 2361-2369.
68. L. J. A. Koster, V. D. Mihailetchi, R. Ramaker and P. W. M. Blom, *Applied Physics Letters*, 2005, **86**, 123509.
69. C. M. Proctor, M. Kuik and T.-Q. Nguyen, *Progress in Polymer Science*, 2013, **38**, 1941-1960.
70. P. E. Keivanidis, G. Itskos, Z. Kan, E. Aluicio-Sarduy, H. Goudarzi, V. Kamm, F. Laquai, W. Zhang, C. Brabec, G. Floudas and I. McCulloch, *ACS Applied Materials & Interfaces*, 2020, **12**, 2695-2707.
71. M. J. Frisch, G. W. Trucks, H. B. Schlegel, G. E. Scuseria, M. A. Robb, J. R. Cheeseman, G. Scalmani, V. Barone, G. A. Petersson, H. Nakatsuji, X. Li, M. Caricato, A. V. Marenich, J. Bloino, B. G. Janesko, R. Gomperts, B. Mennucci, H. P. Hratchian, J. V. Ortiz, A. F. Izmaylov, J. L. Sonnenberg, F. Williams; Ding, F. Lipparini, F. Egidi, J. Goings, B. Peng, A. Petrone, T. Henderson, D. Ranasinghe, V. G. Zakrzewski, J. Gao, N. Rega, G. Zheng, W. Liang, M. Hada, M. Ehara, K. Toyota, R. Fukuda, J. Hasegawa, M. Ishida, T. Nakajima, Y. Honda, O. Kitao, H. Nakai, T. Vreven, K. Throssell, J. A. Montgomery Jr., J. E. Peralta, F. Ogliaro, M. J. Bearpark, J. J. Heyd, E. N. Brothers, K. N. Kudin, V. N. Staroverov, T. A. Keith, R. Kobayashi, J. Normand, K. Raghavachari, A. P. Rendell, J. C. Burant, S. S. Iyengar, J. Tomasi, M. Cossi, J. M. Millam, M. Klene, C. Adamo, R. Cammi, J. W. Ochterski, R. L. Martin, K. Morokuma, O. Farkas, J. B. Foresman and D. J. Fox, *Journal*, 2016.
72. D. Guo, L. Yang, J. Zhao, J. Li, G. He, D. Yang, L. Wang, A. Vadim and D. Ma, *Materials Horizons*, 2021, **8**, 2293-2302.
73. I. Krauhausen, D. A. Koutsouras, A. Melianas, S. T. Keene, K. Lieberth, H. Ledanseur, R. Sheelamanthula, A. Giovannitti, F. Torricelli, I. Mcculloch, P. W. M. Blom, A. Salleo, Y. v. d. Burgt and P. Gkoupidenis, *Science Advances*, 2021, **7**, eabl5068.
74. R. T. Richardson, M. R. Ibbotson, A. C. Thompson, A. K. Wise and J. B. Fallon, *Healthcare Technology Letters*, 2020, **7**, 58-65.
75. S. Esiner, G. W. P. van Pruissen, M. M. Wienk and R. A. J. Janssen, *Journal of Materials Chemistry A*, 2016, **4**, 5107-5114.
76. A. I. Zvyagina, I. N. Meshkov, A. A. Ezhov, A. Shiryaev, Y. G. Gorbunova, K. P. Birin, A. Y. Tsivadze, V. V. Arslanov and M. A. Kalinina, *Colloids and Surfaces A: Physicochemical and Engineering Aspects*, 2016, **509**, 376-383.